ADVANCED MATERIALS
www.advmat.de

Rational Design of Conjugated Photosensitizers with Controllable Photoconversion for Dually Cooperative Phototherapy

Shuyue Ye, Jiaming Rao, Shihong Qiu, Jinglong Zhao, Hui He, Ziling Yan, Tao Yang, Yibin Deng, Hengte Ke, Hong Yang, Yuliang Zhao, Zhengqing Guo,* and Huabing Chen**

High-performance photosensitizers are highly desired for achieving selective tumor photoablation in the field of precise cancer therapy. However, photosensitizers frequently suffer from limited tumor suppression or unavoidable tumor regrowth due to the presence of residual tumor cells surviving in phototherapy. A major challenge still remains in exploring an efficient approach to promote dramatic photoconversions of photosensitizers for maximizing the anticancer efficiency. Here, a rational design of boron dipyrromethene (BDP)-based conjugated photosensitizers (CPs) that can induce dually cooperative phototherapy upon light exposure is demonstrated. The conjugated coupling of BDP monomers into dimeric BDP (*di*-BDP) or trimeric BDP (*tri*-BDP) induces photoconversions from fluorescence to singlet-to-triplet or nonradiative transitions, together with distinctly redshifted absorption into the near-infrared region. In particular, *tri*-BDP within nanoparticles shows preferable conversions into both primary thermal effect and minor singlet oxygen upon near-infrared light exposure, dramatically achieving tumor photoablation without any regrowth through their cooperative anticancer efficiency caused by their dominant late apoptosis and moderate early apoptosis. This rational design of CPs can serve as a valuable paradigm for cooperative cancer phototherapy in precision medicine.

Photosensitizers have extensively explored as emerging versatile compounds in many fields including photodynamic therapy (PDT), photocatalysis, cell signaling, and biosensors.[1] For cancer therapy, excited photosensitizer is able to produce highly cytotoxic reactive oxygen species (ROS) such as singlet oxygen via intersystem crossing (ISC)-mediated singlet-to-triplet transition and subsequent energy transfer, thus causing the apoptosis through the oxidation of biologically relevant molecules in mitochondria and nucleus to cause selective suppression against malignant shallow tumors.[2] PDT possesses several distinct advantages over conventional therapeutics including precise spatiotemporal control, selective treatment with minimized adverse side effect, and negligible drug resistance.[2b,3] To date, several types of organic photosensitizers including boron dipyrromethene (BDP), phthalocyanine, and porphyrin have been extensively developed for achieving effective PDT through versatile strategies such as heavy-atom effect, spin converter, charge recombination, exciton coupling, suppressed photoinduced electron transfer, as well as functional substitution of pH-activatable dimethylaminophenyl group, mitochondria-targeted triphenylphosphonium bromide, or antiangiogenic acetazolamide moiety.[4] Moreover, versatile drug vehicles such as micelles, vesicles, graphene oxide, mesoporous silica nanoparticles, and metal–organic frameworks are frequently utilized to boost their anticancer efficiency through enhanced singlet oxygen generation, self-supplied oxygen, improved resistance to photobleaching, or preferable tumor accumulation.[2b,c,3,4,5] Unfortunately, these photosensitizers frequently suffer from limited tumor suppression or unavoidable tumor regrowth due to the residual tumor cells surviving from light irradiation, usually owing to their several drawbacks including shallow light penetration depth in visible region (frequently less than 650 nm), absolute oxygen dependence, insufficient cytoplasmic drug translocation, and inadequate cell damage from singlet oxygen-mediated apoptosis. Hence, highly potent photosensitizer with distinctly redshifted absorption is highly desired for achieving tumor photoablation.[2b,4b]

S. Y. Ye, Dr. S. H. Qiu, J. L. Zhao, Dr. H. He, Z. L. Yan, T. Yang, Dr. Y. B. Deng, Dr. H. T. Ke, Prof. H. Yang, Prof. H. B. Chen
State Key Laboratory of Radiation Medicine and Protection
Jiangsu Key Laboratory of Neuropsychiatric Diseases, and College of Pharmaceutical Sciences
Soochow University
Suzhou 215123, China
E-mail: hhe@suda.edu.cn; chenhb@suda.edu.cn

J. M. Rao, Dr. Z. Q. Guo, Prof. H. B. Chen
State Key Laboratory of Radiation Medicine and Protection
Collaborative Innovation Center of Radiation Medicine of Jiangsu Higher Education Institutions, and School of Radiation Medicine and Protection
Soochow University
Suzhou 215123, China
E-mail: zqguo@suda.edu.cn

Prof. Y. L. Zhao
CAS Key Laboratory for Biomedical Effects of Nanomaterials and Nanosafety
Center of Excellence for Nanosciences
National Center for Nanoscience and Technology of China
Beijing 100190, China

The ORCID identification number(s) for the author(s) of this article can be found under https://doi.org/10.1002/adma.201801216.

DOI: 10.1002/adma.201801216

In the past few years, many efforts have been made to rationally synthesize efficient photosensitizers toward enhanced singlet oxygen generation for improving their PDT efficacy.[3a–i,6] Some emerging approaches are explored to boost the photoconversions of photosensitizers such as BDP into singlet oxygen through long-lived triplet state, together with reduced radiative transition.[4f] For instance, the intramolecular resonance energy transfer (RET) and resonance energy transfer were exploited to enhance the ISC process and subsequent singlet oxygen generation;[7] Radical enhanced ISC was introduced for causing long-lived triplet state;[8] Photoinduced electron transfer process was also applied to generate locally excited triplet state of heavy atom-free dyes in visible absorption.[9] Although these approaches effectively enhance the singlet oxygen generation of photosensitizers, a facile and efficient approach is highly desired to tune their photoconversion behaviors, thus maximizing the photocytotoxicity to cause potent phototherapy. Previously, we utilized platinum-coordinated BDP to generate both heavy atom effect and nonradiative transition that can cause singlet oxygen and thermal effect for synergistic PDT and photothermal therapy (PTT), implying a possibility to achieve potent phototherapeutic efficacy through maximizing their photoconversions.[10] Herein, we first report a rational design of BDP-based conjugated photosensitizers (CPs) that can induce dually cooperative phototherapy for achieving tumor photoablation surgery upon NIR light exposure (**Figure 1**). The conjugated coupling of BDP monomers into dimeric BDP (*di*-BDP) or trimeric BDP (*tri*-BDP) induces the photoconversions from fluorescence to singlet-to-triplet or nonradiative transition, together with distinctly redshifted absorption into NIR region. In particular, *tri*-BDP within nanoparticles shows the preferable conversions into both primary thermal effect and minor singlet oxygen upon 785 nm light exposure as compared to *di*-BDP with its main conversion into singlet oxygen through ISC, dramatically achieving the total tumor photoablation without any regrowth.

To synthesize BDP-based CPs with tunable photoconversions, the conjugated coupling of BDP monomers into *di*-BDP and *tri*-BDP was designed as depicted in **Figure 2**a. Briefly, the formylation of highly emissive BDP precursor into *β*-formyl BDP (*mono*-BDP), followed by subsequent one-pot Knoevenagel self-condensation reaction that finally afforded the conjugated *di*-BDP and *tri*-BDP. The chemical structures and molecular weights of *mono*-BDP, *di*-BDP, *tri*-BDP, and their precursors were fully characterized using ^{1}H NMR, ^{13}C NMR, and HR-MS analysis (Figures S1–S7, Supporting Information).

To deliver hydrophobic *di*-BDP and *tri*-BDP, they were added into poly(ethylene glycol)$_{114}$-*b*-poly(caprolactone)$_{60}$ copolymer in dimethyl sulfoxide (DMSO), respectively, and then dispersed into distilled water under ultrasonication, followed by the formation of *di*-BDP-loaded nanoparticles (*di*-BDP-NPs) or *tri*-BDP-loaded nanoparticles (*tri*-BDP-NPs) at the loading level of 20% after the purification through the dialysis (Figure 1a). The *mono*-BDP-loaded nanoparticles (*mono*-BDP-NPs) were also prepared as the control using a similar procedure. *di*-BDP-NPs and *tri*-BDP-NPs were observed using transmission electron microscopy (TEM), indicating the spherical morphologies with average diameters of 85.0 ± 6.0 and 69.0 ± 8.0 nm, respectively (Figure 2b; and Figure S8, Supporting Information). Dynamic light scattering (DLS) measurements demonstrate that they possessed the average hydrodynamic diameters of 95.0 and 82.0 nm, respectively (Figure 2c; and Figure S8, Supporting Information), implying their potential passive targeting ability through enhanced permeation and retention (EPR) effect. Free

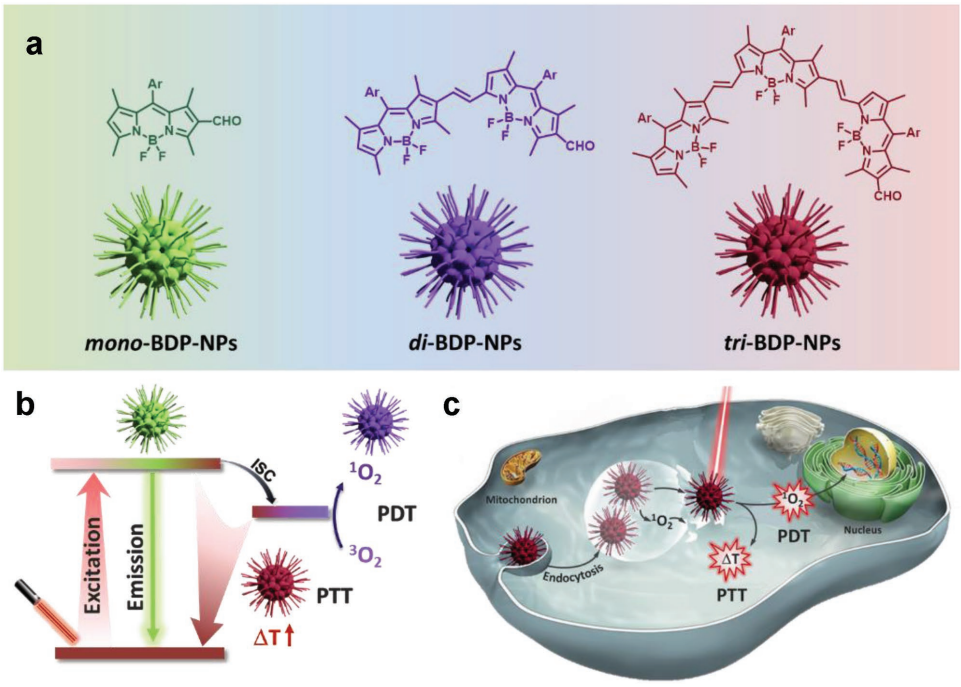

Figure 1. a) Chemical structures and nanoparticles of CPs. b) Photoconversion routes of various CPs. c) Cooperative phototherapy of *tri*-BDP-NPs against tumor cells through PTT/PDT treatments under light exposure.

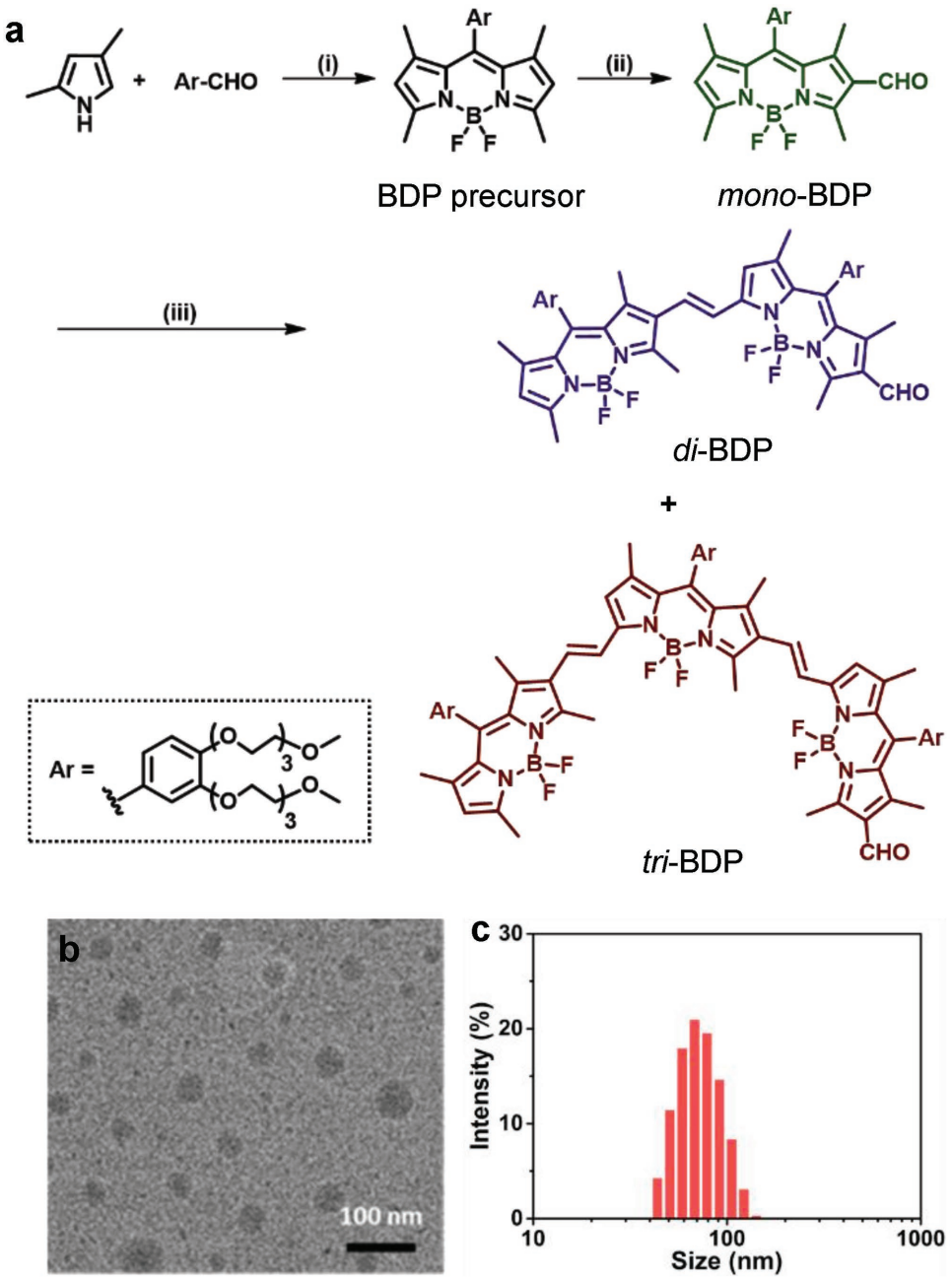

Figure 2. a) Synthetic route of *mono*-BDP, *di*-BDP, and *tri*-BDP. i) TFA, CH_2Cl_2; DDQ; Diisopropylethylamine; $BF_3{\cdot}Et_2O$; ii) $POCl_3$, DMF; iii) HOAc, Piperidine. b) TEM image and c) size distribution of *tri*-BDP-NPs.

di-BDP and *tri*-BDP were also dissolved in aqueous solutions containing 0.5% DMSO as the controls (Figure S8, Supporting Information), respectively, which show broad size distributions due to their aggregations in aqueous solutions.

The absorption spectra of *di*-BDP-NPs and *tri*-BDP-NPs were observed in water. As shown in **Figure 3**a, they displayed the absorption peaks at 649 and 738 nm in water, respectively, while *mono*-BDP-NPs showed an absorption peak at 491 nm. Distinctly, the conjugated coupling of BDP monomers into *di*-BDP or *tri*-BDP caused the distinctly redshifted absorption into visible or NIR region due to the extended delocalized π system. In particular, *tri*-BDP-NPs with NIR absorption might provide deeper light penetration depth for tumor treatment. Moreover, they also showed the broadened absorptions and displayed the redshifts of about 20 nm in their absorption as compared to free *di*-BDP and *tri*-BDP in DMSO, reasonably owing to the formations of their *J*-type and *H*-type aggregates with *di*-BDP or *tri*-BDP aggregates with intermolecular π–π stacking within the nanoparticles.[6,10] These redshifts were further confirmed by their redshifted emission peaks at 756 and 794 nm with large stokes shifts (Figure 3b). Clearly, the conjugated coupling and subsequent *J*-type aggregation of BDP monomers within

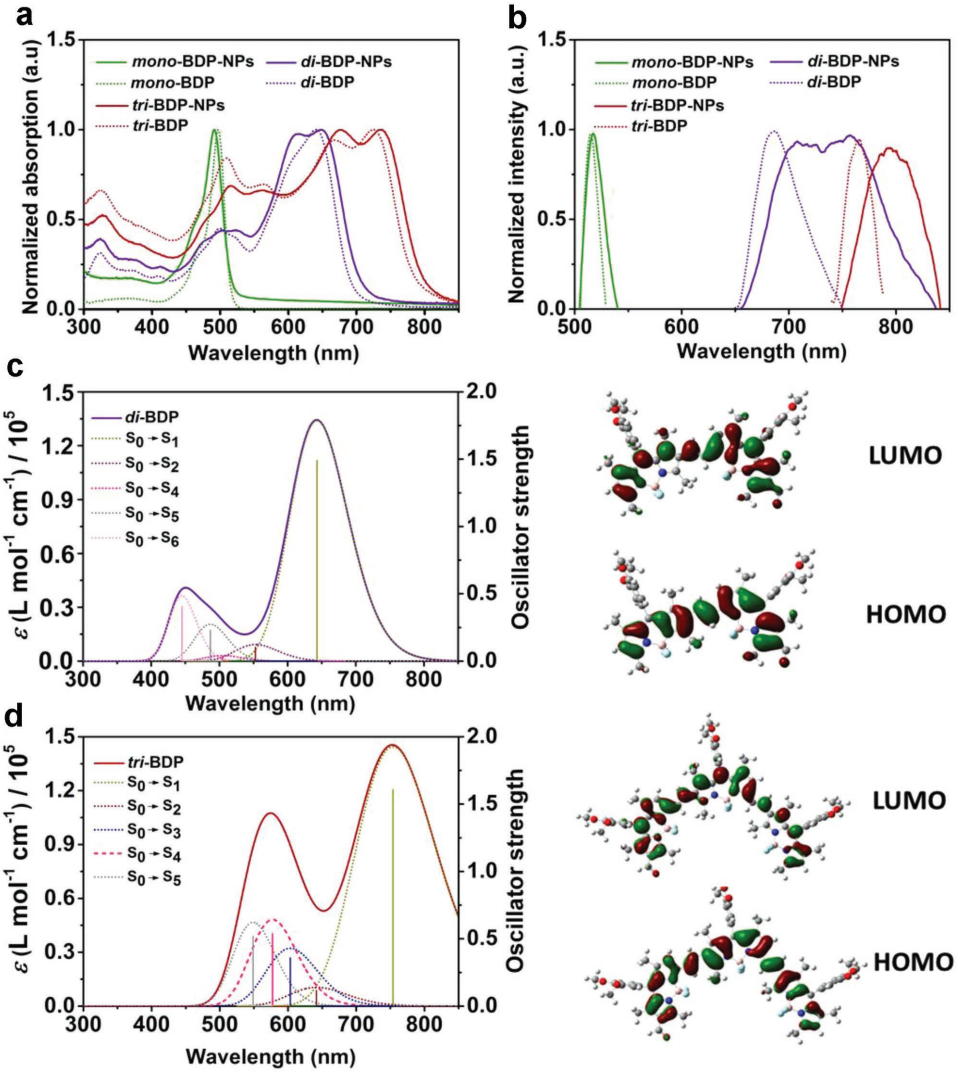

Figure 3. a) Normalized absorption spectra and b) emission spectra of *mono*-BDP-NPs, *di*-BDP-NPs, and *tri*-BDP-NPs as compared to free *mono*-BDP, *di*-BDP, and *tri*-BDP in DMSO. c,d) Calculated UV–vis absorption spectra and HOMO/LUMO of energy-minimized calculated (Gaussian) *di*-BDP (c) and *tri*-BDP (d). Calculation was performed at B3LYP/6-311G* level with Gaussian 09W (Scaling factors are 0.9).

nanoparticles account for their apparently redshifted absorption in a controlled manner.

To illustrate the electronic states of *di*-BDP and *tri*-BDP within the nanoparticles, we carried out the time-dependent density theory (TDDFT) calculation (Figure 3c,d). The calculated UV–vis absorption maxima of *di*-BDP and *tri*-BDP were located at 642 and 752 nm, respectively, which accord well with their experimental absorptions in Figure 3a. Distinctly, the S_1 states in *di*-BDP and *tri*-BDP originate from highest occupied molecular orbitals (HOMO) to lowest unoccupied molecular orbitals (LUMO) with the largest extinction coefficient ($\approx 10^5$ L mol^{-1} cm^{-1}), showing a typical π–π^* characteristics. According to the frontier orbitals of *di*-BDP and *tri*-BDP (Figure 3c,d), the electronic density is delocalized on the backbone of conjugated BDP and thus cause the lower energy gap between HOMO and LUMO in moieties.[11] Moreover, *tri*-BDP possess a narrower energy gap for π–π^* transition due to their larger conjugated π system as compared to *di*-BDP, thus causing their more intensive absorption in NIR region. Apparently, the conjugated coupling of BDP monomers significantly results in the redshifted absorption into NIR region, suggesting that this type of CPs might be excited at redshifted wavelength that depends on their conjugated conformations.

To distinguish the type of ROS from *di*-BDP-NPs and *tri*-BDP-NPs upon light exposure, the electron spin resonance (ESR) was applied using 2,2,6,6-tetramethylpiperide (TEMP) and 5,5-dimethyl-1-pyrroline-*N*-oxide (DMPO) as the spin-trapping adducts (**Figure 4**a). Both of their ESR spectra showed the characteristic 1:1:1 multiplicity from TEMP-1-oxyl after 5 min light exposure, confirming the generation of singlet oxygen from these two nanoparticles.[12] The transient absorption spectra show that *di*-BDP and *tri*-BDP had the triplet lifetimes (τ) of 93.6 and 70.6 µs (Figure 4b), respectively, suggesting that both of them undergo their efficient singlet-to-triplet transition, and *di*-BDP shows a more favorable capacity to produce singlet oxygen as compared to *tri*-BDP.[10] The singlet oxygen generations from *di*-BDP-NPs and *tri*-BDP-NPs were further investigated

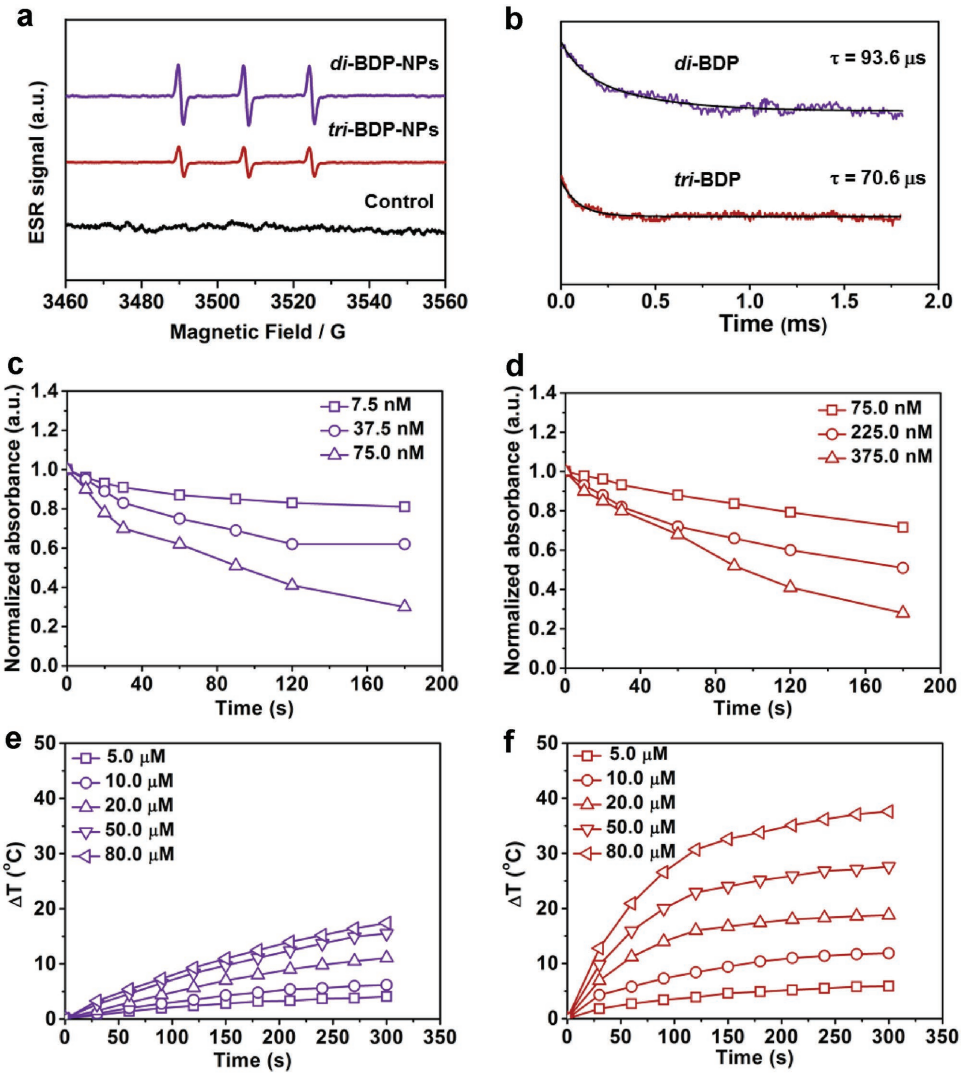

Figure 4. a) ESR spectra of *di*-BDP-NPs and *tri*-BDP-NPs under 660 and 785 nm light exposures at 0.5 W cm^{-2}, respectively. b) Decay trace of *di*-BDP at 660 nm and *tri*-BDP at 780 nm at the excitation of 600 nm in their transient absorption. c,d) Normalized absorbance of DPBF at 410 nm in the solutions of *di*-BDP-NPs (c) and *tri*-BDP-NPs (d) at different concentrations under 660 or 785 nm light exposure at 0.5 W cm^{-2} for 3 min. e,f) Temperature elevations of *di*-BDP-NPs (e) and *tri*-BDP-NPs (f) under 660 or 785 nm light exposure at 0.5 W cm^{-2} for 5 min.

using 1,3-diphenyliso-benzofuran (DPBF) as a probe under light exposure. *di*-BDP-NPs exhibited the distinct concentration-dependent singlet oxygen generation in the range of 7.5–75.0 nmol L^{-1} (Figure 4c), while *tri*-BDP-NPs showed a similar singlet oxygen generation in a much higher concentration range (Figure 4d). Distinctly, *di*-BDP-NPs are able to generate much more singlet oxygen under light exposure as compared to *tri*-BDP-NPs. To further quantify the abilities of *di*-BDP-NPs and *tri*-BDP-NPs to generate singlet oxygen under light exposure, their singlet oxygen quantum yields were also evaluated. They showed the singlet oxygen quantum yields (Φ_Δ) of 0.25 and 0.18 (**Table 1**), respectively, which are higher than those of *mono*-BDP-NPs (Φ_Δ = 0.09), chlorin e6-loaded nanoparticles (Ce6-NPs, Φ_Δ = 0.12), and indocyanine green-loaded nanoparticles (ICG-NPs, Φ_Δ = 0.1, Table S1, Supporting Information). In contrast, free *di*-BDP and *tri*-BDP as the control had the singlet oxygen quantum yields of 0.22 and 0.19 (Table S1, Supporting Information), respectively. Apparently, the encapsulation of *di*-BDP or *tri*-BDP into the nanoparticles shows no significant influence on the singlet oxygen generation, presumably due to the formation of well-organized *J*-type and *H*-type aggregates. Moreover, BDP-based conjugated photosensitizers possess a preferable capacity to generate photothermal conversion and singlet oxygen generation as compared to *mono*-BDP, Ce6,

Table 1. Photoconversion parameters of *mono*-BDP-NPs, *di*-BDP-NPs, and *tri*-BDP-NPs (Φ_Δ: singlet oxygen quantum yield; η_T: photothermal conversion efficiency; Φ_F: fluorescence quantum yield; n. d., none detected).

	tri-BDP-NPs	*di*-BDP-NPs	*mono*-BDP-NPs
Φ_Δ	0.18	0.25	0.09
η_T	45.2%	32.2%	n. d.
Φ_F	9.6×10^{-5}	8.3×10^{-4}	3.2×10^{-2}

and ICG, possibly due to the distinctly reduced fluorescence quantum yield (Table 1). In addition, *di*-BDP-NPs possess a preferable ability to produce singlet oxygen as compared to *tri*-BDP-NPs.

To assess the photothermal conversion capacities of *di*-BDP-NPs and *tri*-BDP-NPs through nonradiative transition, their photothermal conversion efficiencies (η_T) were measured under light exposure at 0.5 W cm^{-2}. *di*-BDP-NPs and *tri*-BDP-NPs exhibited the photothermal conversion efficiencies of 32.2% and 45.2% (Table 1; and Figure S9, Supporting Information), respectively, while no obvious photothermal conversion was observed for *mono*-BDP-NPs, and ICG-NPs and Ce6-NPs only had the photothermal conversions of 26.0% and 14.0% (Table S1, Supporting Information), respectively. Distinctly, the coupling of BDP monomers into *di*-BDP or *tri*-BDP caused their effective photothermal conversion. In particular, *tri*-BDP-NPs exhibit a more significant photothermal conversion as compared to *di*-BDP-NPs under light exposure due to their preferable nonradiative transition and relatively shorter triplet lifetime, and are also comparable to those of the existing photothermal agents such as CuS nanoparticles.[13] Reasonably, the enhanced triplet lifetime might be responsible for the lower photothermal conversion of *di*-BDP-NPs as shown in Figure 4b.

To further evaluate the photothermal conversion, we measured the temperature elevations of *di*-BDP-NPs and *tri*-BDP-NPs under light exposure at 0.5 W cm^{-2} (Figure 4e,f). *tri*-BDP-NPs exhibited the temperature elevation (ΔT) of 38 °C at the concentration of 80.0 μmol L^{-1} in 300 s, and also showed the concentration-dependent temperature elevations (Figure 4f), resulting from their high photothermal conversion efficiency and remarkable absorbance. In contrast, *di*-BDP-NPs had the lower temperature elevations under light exposure as compared to *tri*-BDP-NPs (Figure 4e). Thus, both *di*-BDP-NPs and *tri*-BDP-NPs as a type of CPs afford the dual photoconversions into singlet oxygen and photothermal effect that results from their reduced radiative transition, as further evidenced by their reduced fluorescence quantum yields (Φ_F, Table 1).[10] In particular, *tri*-BDP-NPs with an extendedly conjugated structure primarily hold a preferable photothermal conversion ability together with moderate singlet oxygen generation upon light exposure. Oppositely, *di*-BDP-NPs display a primary singlet oxygen generation accompanied with a minor photothermal conversion due to their favorable ISC-mediated triplet.

The resistances of *di*-BDP-NPs and *tri*-BDP-NPs to photobleaching were observed due to their key role in light treatment. *di*-BDP-NPs and *tri*-BDP-NPs only showed the subtle changes in their absorbance during 16 min under light exposure (Figure S10, Supporting Information), indicating a preferable resistance to photobleaching when compared with free *di*-BDP, free *tri*-BDP, Ce6-NPs, and ICG-NPs as the controls. Clearly, the encapsulation within nanoparticles protects their unsaturated bonds from the damage of radicals in solution for suppressing the photo-oxidation.[14] Moreover, we observed the chemical stability of *di*-BDP-NPs and *tri*-BDP-NPs in aqueous solutions (Figure S11, Supporting Information), suggesting their good chemical stability without any degradation during 48 h.

The cellular uptakes of *di*-BDP-NPs and *tri*-BDP-NPs were investigated on 4T1 tumor cells (**Figure 5**a). They exhibited remarkable increases in their cellular uptakes as compared to free *di*-BDP and *tri*-BDP during 48 h incubation, indicating their preferable endocytosis that is highly favorable for causing subsequent photocytotoxicity. Next, their endocytic pathways were further assessed using various pathway inhibitors (Figure 5b). *di*-BDP-NPs and *tri*-BDP-NPs exhibited the decreases of ≈50% in their cellular uptake in the presence of chlorpromazine, an inhibitor against clathrin-mediated endocytosis, indicating that both of them undergo the clathrin-mediated endocytosis.

To evaluate the photocytotoxicity, *di*-BDP-NPs and *tri*-BDP-NPs were incubated with 4T1 cells for 24 h, followed by 660 and 785 nm light exposures at 0.5 W cm^{-2}, respectively. In the darkness, both *di*-BDP-NPs and *tri*-BDP-NPs showed no significant photocytotoxicity, while they exhibited the IC_{50} values of 0.22 and 1.30 μmol L^{-1} upon 5 min light exposure (Figure 5c,d; and Table S2, Supporting Information), reasonably resulting from both singlet oxygen and photothermal effect. Moreover, the longer light exposure (15 min) further caused the decreases of their IC_{50} values (Figures S12 and S13, Supporting Information), indicating their dependence on light exposure as well. Interestingly, the distinct early apoptosis was responsible for the photocytotoxicity of *di*-BDP-NPs due to their favorable singlet oxygen generation (Figure 5e), while the late apoptosis primarily contributed to that of *tri*-BDP-NPs presumably owing to their preferable photothermal effect-mediated hyperthermia, although both of them have dual photoconversions into both singlet oxygen and photothermal effect. Afterward, to differentiate the photothermal cell damage, the photocytotoxicity of *di*-BDP-NPs and *tri*-BDP-NPs were further investigated against 4T1 cells that were incubated with ROS scavenger Vitamin C (Vc). They only had the IC_{50} values of ≈20.0 and ≈12.0 μmol L^{-1} under 660 and 785 nm light exposures (Figure 5c,d), respectively. Obviously, the PTT damage alone causes the distinctly reduced photocytotoxicity in the absence of singlet oxygen,[10,15] and simultaneously *tri*-BDP-NPs possess a preferable photothermal cytotoxicity as compared to *di*-BDP-NPs owing to their favorable photothermal effect. To further distinguish the role of photodynamic damage in the photocytotoxicity of *di*-BDP-NPs and *tri*-BDP-NPs, we temporarily incubated 4T1 cells at ≈4 °C during light exposure to avoid temperature elevation (Figures S14 and S15, Supporting Information). They showed the IC_{50} values of 0.53 and 34.8 μmol L^{-1} that were caused by the PDT damage alone, respectively. Distinctly, *di*-BDP-NPs show more favorable photodynamic cytotoxicity as compared to *tri*-BDP-NPs. Subsequently, the cooperative index (CI) of *di*-BDP-NPs and *tri*-BDP-NPs were calculated to be 0.42 and 0.15, respectively. It suggests that both of them have the apparently cooperative effect between their PDT and PTT efficiencies (CI <0.8 is considered as cooperative effect),[16] and *tri*-BDP-NPs possess a stronger cooperative phototherapeutic efficiency as compared to *di*-BDP-NPs, owing to their primary late apoptosis and moderate early apoptosis.

To further explore the cooperative mechanism of their photocytotoxicity, the confocal laser scanning microscopy (CLSM) was employed to observe their cytoplasmic translocation behaviors of *di*-BDP-NPs and *tri*-BDP-NPs under light exposure. In the darkness, they showed the colocalization percentages of 93.1% and 94.5% with the lysosomes after 0.5 h incubation due to their effective endocytosis (Figure 5f; and Figure S16, Supporting Information). However, after 5 min light exposure at

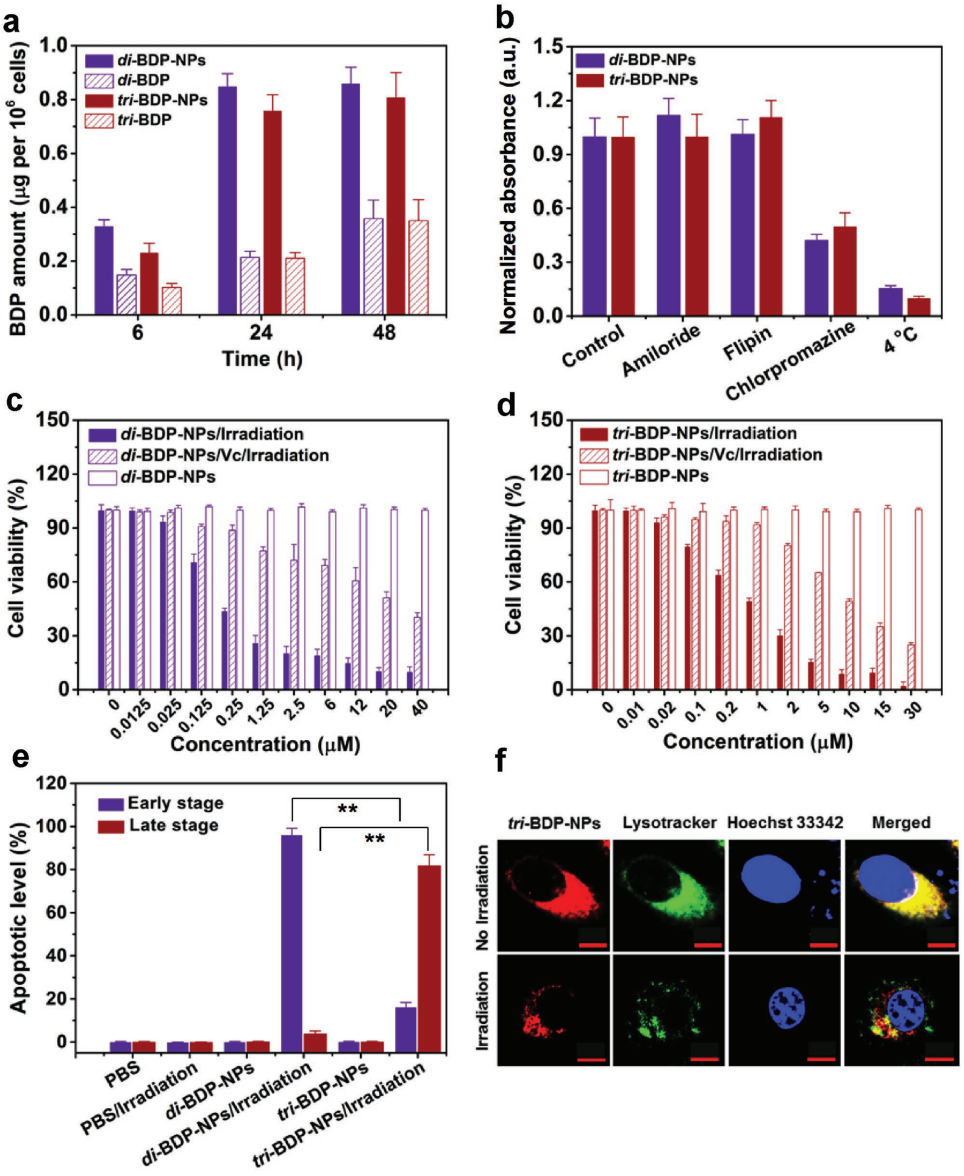

Figure 5. a) Cellular uptake of *di*-BDP-NPs and *tri*-BDP-NPs at the dose of 80.0 μmol L^{-1} by 4T1 cells after 6, 24, and 48 h incubation, respectively. b) Normalized absorbance of *di*-BDP-NPs and *tri*-BDP-NPs internalized by 4T1 tumor cells treated with PBS, amiloride, flipin, and chlorpromazine at 37 °C, and PBS at 4 °C, respectively. c) Relative cell viability of 4T1 tumor cells treated with *di*-BDP-NPs at various doses under 660 nm light exposure at 0.5 W cm^{-2} for 5 min. d) Relative cell viability of 4T1 tumor cells treated with *tri*-BDP-NPs at various doses under 785 nm light exposure at 0.5 W cm^{-2} for 5 min. e) Apoptosis level of 4T1 cells treated with *di*-BDP-NPs and *tri*-BDP-NPs at the dose of 1.0 μmol L^{-1} for 24 h incubation, followed by 660 or 785 nm light exposure at 0.5 W cm^{-2} for 5 min using Annexin V-FITC/PI Apoptosis Detection Kit (Student's *t*-test, $^{**}p < 0.01$). f) CLSM images of 4T1 cells stained by Lysotracker Green DND 26 and Hoechst 33342 after 0.5 h incubation with *tri*-BDP-NPs under 785 nm light exposure at 0.5 W cm^{-2} for 5 min (scale bar, 10 μm).

0.5 W cm^{-2}, their colocalizations were respectively reduced to 71.9% and 65.2%, probably owing to the ROS-mediated lysosomal rupture through photochemical internalization effect, as evidenced by their green fluorescence caused by the lysosomal rupture in the acridine orange (AO) staining (Figure S17, Supporting Information).[10] Apparently, this type of CPs undergo an effective cytoplasmic translocation from the lysosome to cytoplasm in several minutes under light exposure, which might favorably promote their accessibility to nucleus and mitochondria for cooperative photocytotoxicity.[17]

To demonstrate the capacities of *di*-BDP-NPs and *tri*-BDP-NPs to accumulate at tumor sites, their biodistributions were studied in the mice bearing 4T1 tumors at the dose of 8.0 mg kg^{-1}. Both of them exhibited distinctly improved tumor accumulations at 24 h postinjection when compared with free *di*-BDP and *tri*-BDP (**Figure 6**a), indicating that the nanoparticles resulted in the passive tumor targeting through their EPR effect. To evaluate the in vivo hyperthermia at tumor, *di*-BDP-NPs and *tri*-BDP-NPs were intravenously administrated into the mice bearing 4T1 tumor at the dose of 8.0 mg kg^{-1}, respectively, monitored

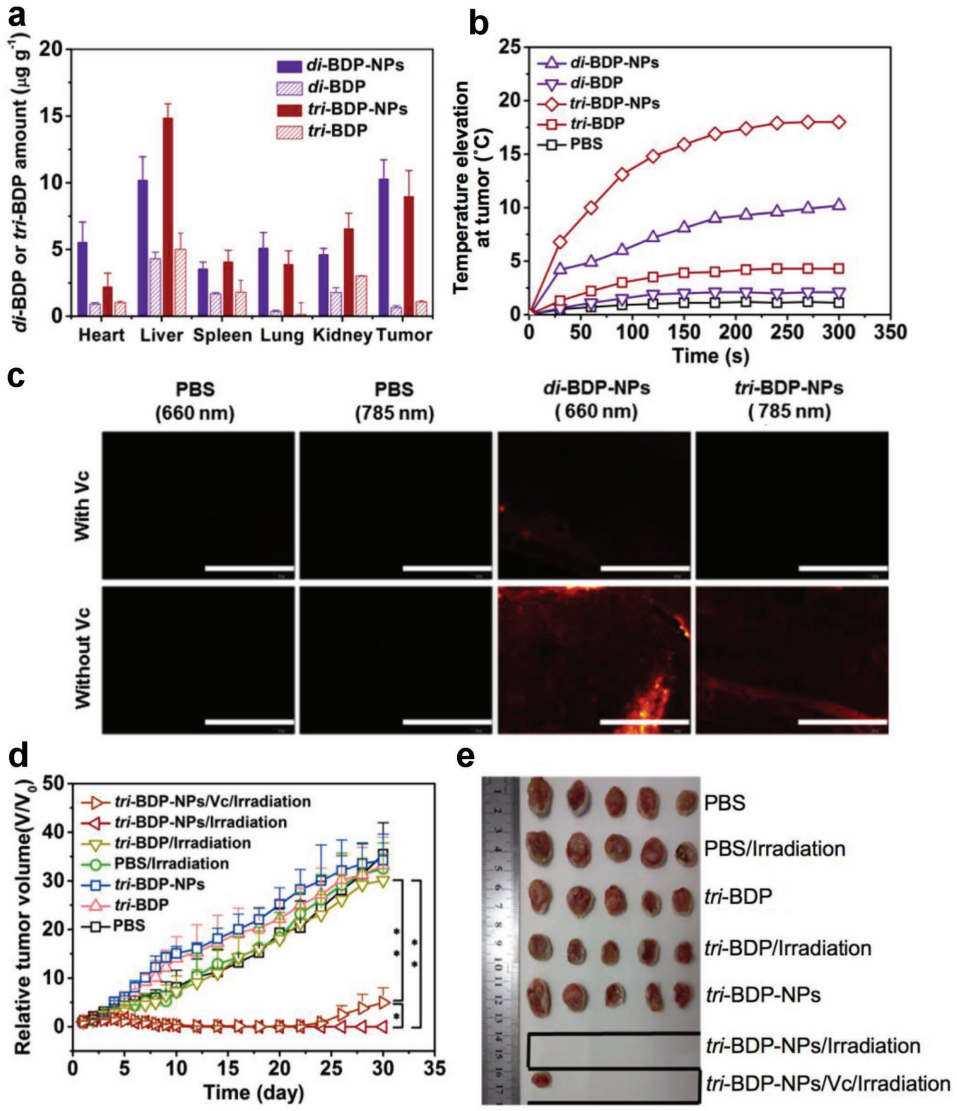

Figure 6. a) Biodistribution of *di*-BDP-NPs and *tri*-BDP-NPs on the mice at 24 h postinjection, respectively. b) Temperature elevation at the tumors of the mice injected with *di*-BDP-NPs and *tri*-BDP-NPs at the dose of 8.0 mg kg^{-1} at 24 h postinjection under 660 or 785 nm light exposure at 0.5 W cm^{-2} for 5 min. c) DHE staining of the tumor sections of the mice treated with *di*-BDP-NPs and *tri*-BDP-NPs at dose of 8.0 mg kg^{-1} in the presence or absence of Vc at 24 h postinjection under 660 or 785 nm light exposure at 0.5 W cm^{-2} for 5 min (Scale bar, 100 μm). d) Tumor growth profile of the mice treated with *tri*-BDP-NPs at the dose of 8.0 mg kg^{-1} in the presence or absence of Vc under 785 nm light exposure at 0.5 W cm^{-2} for 5 min (Student's *t*-test, $*p < 0.05$, and $**p < 0.01$), and e) their tumor photo at the end of the experiment.

by the infrared thermography under 5 min light exposure at 0.5 W cm^{-2} at 24 h postinjection. *di*-BDP-NPs and *tri*-BDP-NPs caused the temperature elevations of 10.2 and 18.0 °C under light exposure, respectively (Figure 6b; and Figure S18, Supporting Information), while free *di*-BDP and *tri*-BDP as the control only resulted in the negligible temperature elevations. Distinctly, *tri*-BDP-NPs possess a preferable ability to generate potent hyperthermia for causing PTT treatment at 785 nm as compared to *di*-BDP-NPs, reasonably owing to their preferable photothermal conversion ability.[18] Moreover, the in vivo singlet oxygen generation was also observed from *di*-BDP-NPs and *tri*-BDP-NPs at the tumors using dihydroethidium (DHE) staining, respectively. Free *di*-BDP and *tri*-BDP showed no fluorescence under light irradiation, suggesting the absence of singlet oxygen at the tumors (Figure 6c). Interestingly, *di*-BDP-NPs had a distinct red fluorescence that was further scavenged by Vc at tumor, while *tri*-BDP-NPs caused a relatively weak red fluorescence (Figure 6c). Clearly, *di*-BDP-NPs effectively produce more intracellular singlet oxygen at tumor site as compared to *tri*-BDP-NPs under light exposure. Thus, *di*-BDP-NPs preferably cause more singlet oxygen at tumor, and *tri*-BDP-NPs primarily result in stronger in vivo hyperthermia, although both of them possess both singlet oxygen and photothermal effect.

To evaluate the in vivo phototherapeutic efficacy, *di*-BDP-NPs and *tri*-BDP-NPs were intravenously injected into the tumor-bearing mice at a single dose of 8.0 mg kg^{-1}, respectively, and then suffered from 660 or 785 nm light irradiation at 0.5 W cm^{-2} for 5 min at 24 h postinjection. To distinguish

the role of PDT, Vc as a ROS scavenger was also intratumorally injected into the tumor before light exposure. The tumor volumes were monitored during subsequent 30 d. As depicted in Figure 6d; and Figure S19 (Supporting Information), phosphate buffer saline (PBS) as a control caused the significant increases of more than ≈30-folds in their tumor volumes despite of light exposure, indicating that the light exposure itself has no obvious influence on the tumor growth. *di*-BDP-NPs and *tri*-BDP-NPs also displayed the similar tumor growth profiles to PBS in the lack of light exposure, suggesting both of them have no significant dark cytotoxicity (Figure 6d; and Figure S19, Supporting Information). Importantly, *tri*-BDP-NPs effectively resulted in the total tumor ablation without any regrowth during 30 d (Figure 6e), while *di*-BDP-NPs also effectively led to the tumor ablation, accompanying with tumor regrowth (Figure S19, Supporting Information). Apparently, *tri*-BDP-NPs possess a preferable ability to totally ablate the tumors upon NIR light exposure when compared with *di*-BDP-NPs. Possibly, the NIR absorption, favorable hyperthermia, moderate singlet oxygen, and cytoplasmic translocation cooperatively contribute to their total tumor ablation through their primary late apoptosis and moderate early apoptosis. Interestingly, both of them also displayed more obvious tumor regrowths in the presence of ROS scavenger Vc, suggesting that the PTT treatment alone causes the survivals of tumor cells due to the absence of PDT treatment. The intracellular singlet oxygen at tumor sites plays a key role in severely injuring the residual tumor cells surviving from the hyperthermia-mediated PTT damage. Obviously, *tri*-BDP-NPs show a distinct cooperative PTT/PDT anticancer efficacy that accounts for the total tumor photoablation. In addition, free *di*-BDP and *tri*-BDP showed a similar tumor growth profiles to PBS, suggesting their poor anticancer efficacy due to the absence of tumor accumulation. Thus, extendedly conjugated *tri*-BDP-NPs effectively achieve the cooperative phototherapy with tumor ablation under NIR light exposure.

To confirm the in vivo photocytotoxicity of *di*-BDP-NPs and *tri*-BDP-NPs, the hematoxylin & eosin (H&E) staining was applied to observe their in vivo injuries against the tumors at the dose of 8.0 mg kg^{-1} at 6 h postirradiation. Both of them resulted in destructive necrosis of tumor cells, while free *di*-BDP and *tri*-BDP only caused the negligible injuries on the tumors (Figure S20, Supporting Information). Distinctly, both *di*-BDP-NPs and *tri*-BDP-NPs are able to cause potent in vivo damage on the tumor cells through their hyperthermia and singlet oxygen, indicating that this type of CPs can act as potent photosensitizers for highly efficient phototherapy. In addition, both of them showed no obvious damage against the normal tissues including heart, liver, spleen, lung, and kidney (Figure S21, Supporting Information), confirming their ability to act as a selective therapeutic modality.

In summary, we first demonstrated a rational design of BDP-based CPs that could produce dually cooperative phototherapy for achieving tumor photoablation surgery upon NIR light exposure. The conjugated coupling of BDP monomers into *di*-BDP or *tri*-BDP caused the photoconversion from fluorescence to intersystem crossing or nonradiative transition, together with distinctly reduced radiative transition and redshifted absorption into NIR region. Upon encapsulation within nanoparticles, both *di*-BDP-NPs and *tri*-BDP-NPs also possessed the collective characteristics for achieving efficient cancer phototherapy including enhanced cellular uptake, effective cytoplasmic translocation, and preferable tumor accumulation. In particular, *di*-BDP-NPs might behave as an effective CPs with enhanced triplet state that displays a primary singlet oxygen generation under 660 nm light exposure, while *tri*-BDP-NPs with extendedly conjugated structure primarily hold a preferable photothermal effect under 785 nm light exposure together with moderate singlet oxygen generation, thereby achieving the tumor photoablation surgery without any regrowth through both primary late apoptosis and moderate early apoptosis. This therapeutic benefit is possibly caused by several advantages of CPs including deeper light penetration depth due to distinctly redshifted absorption, improved resistance to photobleaching, reduced oxygen depletion, cytoplasmic drug translocation, as well as combination of late and early apoptosis. Moreover, this approach might avoid the use of heavy atoms such as I, Br, and Pt in conventional strategies that might potentially cause safety concern,[4f] and also suggests a preferably concise regime to synthesize potent CPs with tunable photoconversions, as compared to sophisticated design of donor–acceptor-type conjugated macromolecules with phototherapy. This type of CPs shows an emerging potential to fabricate highly potent photosensitizers with distinctly redshifted absorption, and we believe that this rational design can serve as a valuable paradigm for cooperative cancer phototherapy in precision medicine.

Experimental Section

Detailed experimental materials and methods can be found in the Supporting Information.

Supporting Information

Supporting Information is available from the Wiley Online Library or from the author.

Acknowledgements

S.Y.Y., J.M.R., S.H.Q., and J.L.Z. contributed equally to this work. This work was supported by National Basic Research Program (No. 2014CB931900), National Natural Science Foundation of China (Nos. 51473109, 31671016, 31771089, 21401136, and 81402779), 2017 National Level of Innovation and Entrepreneurship Training Program for College Students (No. 201710285046Z), and Priority Academic Program Development of Jiangsu Higher Education Institutions (PAPD). The animal protocols used in this study were approved by Dr. Xuechu Zhen, chairman of the College Review Committees of Soochow University for animal use and welfare.

Conflict of Interest

The authors declare no conflict of interest.

Keywords

boron dipyrromethene, conjugated photosensitizers, near-infrared absorption, photodynamic therapy, photothermal therapy

Received: February 24, 2018
Revised: April 19, 2018
Published online:

[1] a) O. Planas, N. Macia, M. Agut, S. Nonell, B. Heyne, *J. Am. Chem. Soc.* **2016**, *138*, 2762; b) H. Takeda, K. Ohashi, A. Sekine, O. Ishitani, *J. Am. Chem. Soc.* **2016**, *138*, 4354; c) M. Westberg, L. Holmegaard, F. M. Pimenta, M. Etzerodt, P. R. Ogilby, *J. Am. Chem. Soc.* **2015**, *137*, 1632; d) H. Kim, J. Lee, C. Oh, J. H. Park, *Nat. Commun.* **2017**, *8*, 15880; e) J. Conde, N. Oliva, Y. Zhang, N. Artzi, *Nat. Mater.* **2016**, *15*, 1128.

[2] a) Y. Li, T. Y. Lin, Y. Luo, Q. Liu, W. Xiao, W. Guo, D. Lac, H. Zhang, C. Feng, S. Wachsmann-Hogiu, J. H. Walton, S. R. Cherry, D. J. Rowland, D. Kukis, C. Pan, K. S. Lam, *Nat. Commun.* **2014**, *5*, 4712; b) S. S. Lucky, K. C. Soo, Y. Zhang, *Chem. Rev.* **2015**, *115*, 1990; c) L. Colombeau, S. Acherar, F. Baros, P. Arnoux, A. M. Gazzali, K. Zaghdoudi, M. Toussaint, R. Vanderesse, C. Frochot, *Top. Curr. Chem.* **2016**, *370*, 113.

[3] a) A. Kamkaew, S. H. Lim, H. B. Lee, L. V. Kiew, L. Y. Chung, K. Burgess, *Chem. Soc. Rev.* **2013**, *42*, 77; b) Y. Cheng, H. Cheng, C. Jiang, X. Qiu, K. Wang, W. Huan, A. Yuan, J. Wu, Y. Hu, *Nat. Commun.* **2015**, *6*, 8785; c) Z. Mahmood, J. Zhao, *Photochem. Photobiol. Sci.* **2016**, *15*, 1358; d) Z. Wang, J. Zhao, *Org. Lett.* **2017**, *19*, 4492; e) L. Huang, Z. Li, Y. Zhao, Y. Zhang, S. Wu, J. Zhao, G. Han, *J. Am. Chem. Soc.* **2016**, *138*, 14586; f) E. Özcan, K. Gürkan, B. Topaloğlu, E. T. Eçik, A. Dere, F. Yakuphanoglu, C. Bünyemin, *New J. Chem.* **2018**, *42*, 4972; g) T. Sun, X. Guan, M. Zheng, X. Jing, Z. Xie, *ACS Med. Chem. Lett.* **2015**, *6*, 430; h) X. D. Jiang, X. Liu, T. Fang, C. Sun, *Dyes Pigm.* **2017**, *146*, 438; i) J. Zou, Z. Yin, K. Ding, Q. Tang, J. Li, W. Si, J. Shao, Q. Zhang, W. Huang, X. Dong, *ACS Appl. Mater. Interfaces* **2017**, *9*, 32475.

[4] a) C. Conte, S. Maiolino, D. S. Pellosi, A. Miro, F. Ungaro, F. Quaglia, *Top. Curr. Chem.* **2016**, *370*, 61; b) Z. Zhou, J. Song, L. Nie, X. Chen, *Chem. Soc. Rev.* **2016**, *45*, 6597; c) H. S. Jung, J. Han, H. Shi, S. Koo, H. Singh, H. J. Kim, J. L. Sessler, J. Y. Lee, J. H. Kim, J. S. Kim, *J. Am. Chem. Soc.* **2017**, *139*, 7595; d) J. Tian, L. Ding, H. J. Xu, Z. Shen, H. Ju, L. Jia, L. Bao, J. S. Yu, *J. Am. Chem. Soc.* **2013**, *135*, 18850; e) A. M. Durantini, L. E. Greene, R. Lincoln, S. R. Martinez, G. Cosa, *J. Am. Chem. Soc.* **2016**, *138*, 1215; f) J. Zhao, K. Xu, W. Yang, Z. Wang, F. Zhong, *Chem. Soc. Rev.* **2015**, *44*, 8904.

[5] a) N. M. Idris, M. K. Gnanasammandhan, J. Zhang, P. C. Ho, R. Mahendran, Y. Zhang, *Nat. Med.* **2012**, *18*, 1580; b) Z. Zhou, J. Song, R. Tian, Z. Yang, G. Yu, L. Lin, G. Zhang, W. Fan, F. Zhang, G. Niu, L. Nie, X. Chen, *Angew. Chem., Int. Ed. Engl.* **2017**, *56*, 6492; c) E. Secret, M. Maynadier, A. Gallud, A. Chaix, E. Bouffard, M. Gary-Bobo, N. Marcotte, O. Mongin, K. El Cheikh, V. Hugues, M. Auffan, C. Frochot, A. Morere, P. Maillard, M. Blanchard-Desce, M. J. Sailor, M. Garcia, J. O. Durand, F. Cunin, *Adv. Mater.* **2014**, *26*, 7643; d) K. Lu, C. He, W. Lin, *J. Am. Chem. Soc.* **2015**, *137*, 7600.

[6] H. Lu, J. Mack, Y. Yang, Z. Shen, *Chem. Soc. Rev.* **2014**, *43*, 4778.

[7] a) C. Zhang, J. Zhao, S. Wu, Z. Wang, W. Wu, J. Ma, S. Guo, L. Huang, *J. Am. Chem. Soc.* **2013**, *135*, 10566; b) L. Huang, Z. Li, Y. Zhao, J. Yang, Y. Yang, A. I. Pendharkar, Y. Zhang, S. Kelmar, L. Chen, W. Wu, J. Zhao, G. Han, *Adv. Mater.* **2017**, *29*, 1604789.

[8] Z. Wang, J. Zhao, A. Barbon, A. Toffoletti, Y. Liu, Y. An, L. Xu, A. Karatay, H. G. Yaglioglu, E. A. Yildiz, M. Hayvali, *J. Am. Chem. Soc.* **2017**, *139*, 7831.

[9] a) M. A. Filatov, S. Karuthedath, P. M. Polestshuk, H. Savoie, K. J. Flanagan, C. Sy, E. Sitte, M. Telitchko, F. Laquai, R. W. Boyle, M. O. Senge, *J. Am. Chem. Soc.* **2017**, *139*, 6282; b) X. F. Zhang, X. Yang, B. Xu, *Phys. Chem. Chem. Phys.* **2017**, *19*, 24792.

[10] Z. Guo, Y. Zou, H. He, J. Rao, S. Ji, X. Cui, H. Ke, Y. Deng, H. Yang, C. Chen, Y. Zhao, H. Chen, *Adv. Mater.* **2016**, *28*, 10155.

[11] M. R. Momeni, A. Brown, *J. Chem. Theory Comput.* **2015**, *11*, 2619.

[12] a) T. Yang, L. Liu, Y. Deng, Z. Guo, G. Zhang, Z. Ge, H. Ke, H. Chen, *Adv. Mater.* **2017**, *29*, 1700487; b) L. Zang, G. Cosma, H. Gardner, V. Vallyathan, *Biochim. Biophys. Acta* **1998**, *1425*, 469.

[13] a) T. Yang, Y. Wang, H. Ke, Q. Wang, X. Lv, H. Wu, Y. Tang, X. Yang, C. Chen, Y. Zhao, H. Chen, *Adv. Mater.* **2016**, *28*, 5923; b) H. Luo, Q. Wang, Y. Deng, T. Yang, H. Ke, H. Yang, H. He, Z. Guo, D. Yu, H. Wu, H. Chen, *Adv. Funct. Mater.* **2017**, *27*, 1702834.

[14] a) M. Guo, H. J. Mao, Y. L. Li, A. J. Zhu, H. He, H. Yang, Y. Y. Wang, X. Tian, C. C. Ge, Q. L. Peng, X. Y. Wang, X. L. Yang, X. Y. Chen, G. Liu, H. B. Chen, *Biomaterials* **2014**, *35*, 4656; b) H. He, S. Ji, Y. He, A. Zhu, Y. Zou, Y. Deng, H. Ke, H. Yang, Y. Zhao, Z. Guo, H. Chen, *Adv. Mater.* **2017**, *29*, 1606690; c) G. Hong, S. Diao, A. L. Antaris, H. Dai, *Chem. Rev.* **2015**, *115*, 10816.

[15] a) X. J. Song, Q. Chen, Z. Liu, *Nano Res.* **2015**, *8*, 340; b) L. Cheng, C. Wang, L. Z. Feng, K. Yang, Z. Liu, *Chem. Rev.* **2014**, *114*, 10869.

[16] X. An, A. Zhu, H. Luo, H. Ke, H. Chen, Y. Zhao, *ACS Nano* **2016**, *10*, 5947.

[17] N. Nishiyama, A. Iriyama, W. D. Jang, K. Miyata, K. Itaka, Y. Inoue, H. Takahashi, Y. Yanagi, Y. Tamaki, H. Koyama, K. Kataoka, *Nat. Mater.* **2005**, *4*, 934.

[18] a) R. Gui, A. Wan, X. Liu, W. Yuan, H. Jin, *Nanoscale* **2014**, *6*, 5467; b) A. J. Zhu, K. Miao, Y. B. Deng, H. T. Ke, H. He, T. Yang, M. Guo, Y. L. Li, Z. Q. Guo, Y. Y. Wang, X. L. Yang, Y. L. Zhao, H. B. Chen, *ACS Nano* **2015**, *9*, 7874; c) Y. L. Li, Y. B. Deng, X. Tian, H. T. Ke, M. Guo, A. J. Zhu, T. Yang, Z. Q. Guo, Z. S. Ge, X. L. Yang, H. B. Chen, *ACS Nano* **2015**, *9*, 9626.